eprints@whiterose.ac.uk
https://eprints.whiterose.ac.uk/

Accepted Manuscript

Title: Predictive process parameter selection for Selective Laser Melting Manufacturing: applications to high thermal conductivity alloys

Authors: Priyanshu Bajaj, Jonathan Wright, Iain Todd, Eric A. Jägle
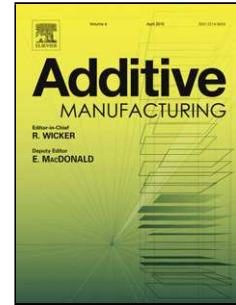
Please cite this article as: Bajaj P, Wright J, Todd I, Jägle EA, Predictive process parameter selection for Selective Laser Melting Manufacturing: applications to high thermal conductivity alloys, *Additive Manufacturing* (2018), https://doi.org/10.1016/j.addma.2018.12.003

Predictive process parameter selection for Selective Laser Melting Manufacturing: applications to high thermal conductivity alloys

Priyanshu Bajaj[1*], Jonathan Wright[2], Iain Todd[2], Eric A. Jägle[1]

[1] Max-Planck-Institut für Eisenforschung GmbH, Max-Planck-Strasse 1, 40237 Düsseldorf, Germany
[2] Department of Materials Science and Engineering, University of Sheffield, Sir Robert Hadfield Building, Mappin Street, S1 3JD, Sheffield, UK

* corresponding author: p.bajaj@mpie.de

Graphical abstract
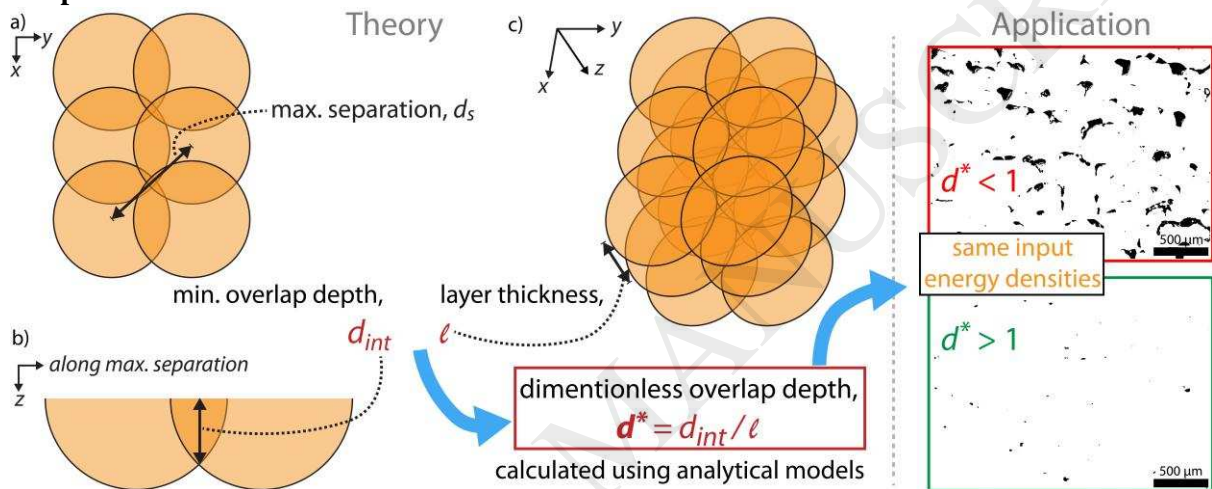
Abstract

There is growing interest in Laser Powder Bed Fusion (L-PBF) or Selective Laser Melting (SLM) manufacturing of high conductivity metals such as copper and refractory metals. SLM manufacturing of high thermal conductivity metals is particularly difficult. In case of refractory metals, the difficulty is amplified because of their high melting point and brittle behaviour. Rapid process development strategies are essential to identify suitable process parameters for achieving minimum porosities in these alloys, yet current strategies suffer from several limitations. We propose a simple approach for rapid process development using normalized process maps. Using plots of normalized energy density vs. normalized hatch spacing, we identify a wide processability window. This is further refined using analytical heat transfer models to predict melt pool size. Final optimization of the parameters is achieved by experiments based on statistical Design of Experiments concepts. In this article we demonstrate the use of our proposed approach for development of process parameters (hatch spacing, layer thickness, exposure time and point distance) for SLM manufacturing of molybdenum and aluminium. Relative densities of 97.4% and 99.7% are achieved using 200 W pulsed laser and 400 W continuous laser respectively, for molybdenum and aluminium, demonstrating the effectiveness of our approach for SLM processing of high conductivity materials.

1. Introduction

Selective Laser Melting (SLM) is a powder bed AM process that utilizes a high power-density laser to selectively melt thin powder layers one by one to produce a three-dimensional component. It is one of the most popular of the AM processes. A detailed description of the process can be found elsewhere [1–4]. SLM systems can be broadly divided into two categories depending on how the laser moves during a scan. The first are continuous systems, where the laser continuously moves along the scan path with a constant velocity and power [1–3]. The second are pulsed-laser systems, where the laser is stagnant when shining over a given spot, shuts off, moves to the next spot, and turns on again [4,5]. The SLM process has been successfully developed for a number of materials including titanium alloys, stainless steels and nickel alloys producing components with a relative density greater than 98% [1–3]. To achieve such high densities, the melt pool generated on exposure to the laser should completely wet the substrate or previously solidified metal before solidification [4,6]. The heat supplied by the laser should be at least the sum of energy lost by laser reflection, required to melt the desired volume, raise the temperature of the melt pool to sustain it long enough that it wets the substrate, and other energy losses.

The conventional approach to finding operable process parameters involves trial and error, experimenting with a large range of process parameters. This is time consuming, expensive, and often does not result in the best parameter set. In recent times, interest has increased in developing SLM process for materials such as copper, aluminium, and, in particular, refractory metals [4,6–9]. The thermal conductivity of these materials is roughly an order of magnitude higher than that of stainless steel and titanium, which can be processed well in SLM. In high-conductivity materials, heat extraction via conduction from the melt pool is fast, and energy loss due to the associated high reflectivity of the material is high. This leads to a small process window due to several detrimental mechanisms: Rapid cooling rates often do not allow enough time for the molten metal to flow. This, coupled with a high surface tension of molten metal results in a phenomenon called 'balling', where the metal solidifies as a globular bead leaving large spaces between itself and previously solidified material, resulting in high porosity [4,7,10]. High thermal gradients develop during the process, which result in large residual stresses. This may lead to crack generation. To tackle these issues we propose a more predictive approach to finding ideal process parameters to achieve minimum porosity. The voids observed in this work are of the well-described lack-of-bonding, gas porosity as well as cracking type [11].

Researchers have proposed multiple methods to predict the range of processing parameters that could be used for a given combination of process and material. The most simplistic approach, that does not account for any heat loss and does not include information about the material, is based on the supplied 'energy density' per unit volume [12,13]. Li et al. describe this volumetric energy density, E_o, as $E_o = \frac{Q}{v\,h\,l}$, where Q and v are laser power and velocity respectively. l is layer thickness and h is the hatch spacing between the tracks [12]. Thomas [14] and Ion [15] suggest the use of normalized process maps, where normalized energy input, $E_o^* = \frac{n\,Q}{2\,v\,l\,h\,\rho\,C_p\,(T_m - T_o)}$ is plotted in terms of process variables, $\frac{r_b}{h}$. Here, $n, \rho, C_p,$ and T_m are the material properties - laser absorptivity, density, specific heat capacity, and melting temperature, respectively, and T_o is the ambient temperature. These maps allow transferring known process windows for one material to a new one. However, they only give a relatively wide processing window, which needs to be further optimized.

2

For better precision in predicting process parameters, numerical Finite Element Models (FEM) have been developed that include all relevant heat loss mechanisms [16–18]. These simulations are computationally expensive and require extensive experimentation for validation of the models themselves. An intermediate approach is to develop analytical models to understand heat transfer during AM processes [19,20]. Analytical models that predict the temperature rise when heating a body using a small heat source, such as a laser, already exist [21–25]. Such models have been used to compute temperature fields during welding [21,22]. It is possible to expand these models to predict the geometry, in particular, the size of the melt pool generated during the SLM process by considering the melting temperature isotherm.

In this paper, we discuss the application of existing analytical heat transfer models to the conditions prevailing during SLM of high- and low-conductivity metals. We then present a simplified predictive approach to process development for SLM of new metals. It involves firstly identifying a wide processability window based on normalized process maps. Secondly, analytical heat transfer models are utilised to narrow down this window. Finally, an experimental process parameter optimization based on Design of Experiments (DOE) principles is performed. We apply our approach to the SLM process development for a refractory metal, molybdenum, and for a very dilute (>99 wt% Al) aluminium alloy. After process parameter optimization, we achieve a relative density of 97.4% for molybdenum, which is considerably higher than previous works using a similar laser power [13], and 99.7% for the aluminium alloy.

2. Methods and procedures

2.1 Laser absorptivity modelling

An important parameter in analytical heat transfer models for SLM is the laser absorptivity of the powder, n. It is defined as the fraction of incident laser power that is absorbed by the material. An empirical relation given by Bramson [26] (Eq. 1) relates laser absorptivity of bulk material, n_s, with the wavelength of the incident laser, λ, and the electrical resistivity of the material, μ [27].

$$n_s = 0.365\sqrt{\frac{\mu}{\lambda}} - 0.0667\left(\frac{\mu}{\lambda}\right) + 0.006\sqrt{\left(\frac{\mu}{\lambda}\right)^3} \qquad \text{Eq. 1}$$

However, this equation ignores surface effects, and metal powders display a higher laser absorptivity value than the bulk material owing to the multiple reflections between powder particles [28]. Boley et al. calculated the laser absorptivity of metal powders using ray-trace simulations (Figure 1) [28]. We define a multiplicity factor, m, such that the laser absorptivity of the powder, n, is given by $n = m \cdot n_s$. We fit a regression equation, $m = 1.0383\, n_s^{-0.487}$, to Boley et al.'s data, relating the multiplicity factor, m, to the laser absorptivity of the bulk material, n_s. In the remainder of this work, we first calculate n_s using Eq. 5 and then obtain n from our regression equation. Note that this treatment ignores the temperature dependence of the absorptivity as well as its change upon melting. This often used simplification was adopted to keep the problem tractable with analytical models, as detailed in the next section.

2.2 Heat transfer modelling

The general differential equation for heat transfer in a stationary, homogeneous, isotropic solid is given as [29]

$$k \left(\frac{\partial^2 T}{\partial x^2} + \frac{\partial^2 T}{\partial y^2} + \frac{\partial^2 T}{\partial z^2} \right) + g = \rho \, C_p \frac{\partial T}{\partial t} \qquad \text{Eq. 2}$$

Here, k is the thermal conductivity of the material and g is heat generation within the solid. The differential equation for heat transfer is composed of three terms: The first term describes the heat transfer within the solid and to or from its boundary surfaces, the second term describes the heat generation within the solid; for SLM this is the absorbed laser power, $n \cdot Q$. The third term describes the heat energy stored within the solid. Analytical solutions for predicting the temperature rise during laser heating are derived from this basic differential equation by setting boundary conditions to simplify the equation from five variables (x,y,z,t,T) to two or three variables [19,22,29,30].

A commonly used solution for predicting temperature profiles during SLM processing is based on the early work of Rosenthal [21,22,27]. This solution is derived for a point heat source moving at a constant velocity, v, over an infinitely large substrate. It assumes a moving coordinate system, such that the origin is always at the location of the heat source, by substituting $x = -v\, t$ [22], where t is time. Due to the assumption of a point heat source, the Rosenthal solution can only be used if the beam radius, r_b, is significantly smaller than the distance the heat can diffuse through during the interaction time, $r_o = \sqrt{4\,\alpha\,t_e}$ [15], i.e. $r_b \ll r_o$. Here, α is the thermal diffusivity of the material. The laser interaction time, t_e, is defined as $t_e = {r_b}/{v}$ for a laser system with constant power output (a continuous system). For pulsed laser systems, t_e is equal to the exposure time. The distance between two laser spots in a pulsed-laser system (point distance, p) has to meet an analogous criterion, $p \ll r_o$. Under such conditions in a pulsed system, the laser can be approximated as moving continuously with an apparent velocity, $v_{app} = \frac{p}{t_e + t_r}$, and apparent laser power, $Q_{app} = \frac{Q\,t_e}{t_e + t_r}$, where t_r is travel time for idle laser between two consecutive exposed points. Under these assumptions, the general heat transfer differential equation (Eq. 2) can be solved to yield the temperature field [21,22]

$$T(x,d) = T_o + \frac{nQ}{2\pi k d} \, exp - \left(\frac{v(x+d)}{2\alpha} \right), \qquad \text{Eq. 3}$$

where
$$d = \sqrt{x^2 + y^2 + z^2}. \qquad \text{Eq. 4}$$

Another solution of Eq. 2 that can be applicable for use in pulsed laser systems is the "1D model". It is derived for an infinitely large static laser shining over an infinitely thick substrate (Eq. 5 and Eq. 6) [19,23]. Here, the heat transfer along x and y directions is ignored and only one dimensional heat flow along the z axis is considered. This solution is valid when the beam radius is much larger than the distance the heat can diffuse through during the interaction time ($r_b \gg r_o$).

$$T = \frac{nQ}{\pi r_b^2 k} \left[\sqrt{\frac{4\alpha t}{\pi}} e^{-[z/(2\sqrt{\alpha t})]^2} - z\, erfc\left(\frac{z}{2\sqrt{\alpha t}} \right) \right] + T_o \qquad (\text{for } t \le t_e) \qquad \text{Eq. 5}$$

$$T = \frac{nQ}{\pi r_b^2 k} \left\{ \sqrt{\frac{4\alpha t}{\pi}} e^{-[z/(2\sqrt{\alpha t})]^2} - \sqrt{\frac{4\alpha(t-t_e)}{\pi}} e^{-[z/(2\sqrt{\alpha(t-t_e)})]^2} - \right.$$
$$\left. z \left[erfc\left(\frac{z}{2\sqrt{\alpha t}} \right) erfc\left(\frac{z}{2\sqrt{\alpha(t-t_e)}} \right) \right] \right\} \qquad (\text{for } t > t_e) \qquad \text{Eq. 6}$$

Based on the prevailing conditions for a material and process combination, one or the other of these models is appropriate. The selected model can then be used to predict the melt pool depth, R_m, by solving the equation for highest value of z at $T = T_m$. For high conductivity materials, r_o is large (since α is high), therefore the Rosenthal solution can be used under most process conditions. For a pulsed laser system, we can assume that the melt pool is hemispherical, while in a continuous system, it can only be assumed to be semi-circular in the $y - z$ plane.

4

To get fully dense components, each melt pool should completely overlap with the previously generated melt pool adjacent to it. To achieve this complete overlap, the minimum overlap depth, d_{int}, (as defined in Figure 2) should be greater than the layer thickness, l. To calculate d_{int}, we consider the maximum lateral separation between two melt pools, which is $d_s = h$ (the hatch distance) for continuous laser systems and $d_s = \sqrt{h^2 + p^2}$ for pulsed laser systems. Using the simulated value for melt pool depth, R_m, the minimum overlap depth can be geometrically calculated as $d_{int} = \sqrt{R_m^2 - \frac{d_s^2}{4}}$ (cf. Figure 2).

We define the dimensionless overlap depth, d^*, as $d^* = {d_{int}}/{l}$. For a given material, d^* is essentially a function of the process parameters - Q, t_e, h, p and l. Note that reasonable assumptions for all but one of these parameters need to be made to be able to calculate the last one given a certain d^* value, e.g. values for Q, h, p and l need to be set to be able to optimize t_e. Many different such parameter combinations lead to the same value of d^*. Under ideal conditions, ignoring the effects of balling and thermal residual stresses, a d^* value of one or more alone should give complete overlap of the melt pools, and therefore lead to high-density components, notwithstanding the parameter combination that was used to arrive at the value of d^*. Figure 3 shows a flow chart depicting our proposed approach under ideal conditions.

For materials that are very sensitive to thermal residual stresses or balling, however, only certain parameter combinations that yield $d^* > 1$ lead to defect-free parts, and additional optimization of process parameters is required. We develop such a method for parameter optimization in section 3.3 using the example of pure Molybdenum.

2.3 Experimental

99.95% pure plasma-spheroidised molybdenum powder supplied by Tekna Advanced Materials Inc., Canada, was used as the feedstock material. Figure 4 shows an SEM (secondary electron) image of the powder and the particle size distribution measured using a Mastersizer 2000 laser diffraction analyser (Malvern Instruments, UK). A Renishaw SLM 125 machine (Renishaw plc, UK) which uses a pulsed laser with a beam radius, r_b, of 25 μm for the no focus offset condition and an idle laser velocity (i.e. jump between spot irradiations) of 2.5 ms^{-1} was used for sample production. Cubic parts with 5 mm edge length were built on a 20 mm thick stainless steel substrate. Additionally, single track trials were conducted by laying a thin layer of molybdenum powder on a 0.5 mm thick, 99.95% pure molybdenum plate (Alfa Aesar, USA) placed on a 20 mm thick stainless steel substrate. All experiments were performed in an argon atmosphere with the oxygen level kept steady at 1000 ppm. Except for the remelting in trial 4, where a laser focus offset of "4", giving a beam radius of 70 μm was used, all experiments were performed in the no focus offset condition. The meander scan strategy with a layer-to-layer rotation angle of 67° was used in all experiments performed in this study to minimize residual stress development [4]. An Aconity 3D Mini from Aconity GmbH, Aachen, Germany, equipped with a continuous laser was used for Al-Sc alloy; detailed experimental information for this alloy is given in the supplementary section.

Based on the discussion by Spierings et al. [2], we selected the optical method for density measurements. Samples were prepared along a plane parallel to the build direction using usual metallographic techniques. Omnimet modular imaging software (Buehler, USA) connected with a Nikon Eclipse LV 150 optical microscope was used for the analysis. The measurements were done at 50x magnification. For each processing condition, three micrographs, including almost the entire sample surface, were taken. Between each measurement, the samples were re-ground and re-polished to reveal a different cross section plane. Each given porosity value is an average of three such

measurements. Philips XL 30 S-FEG scanning electron microscope in secondary electron mode at an accelerating voltage of 20 kV was used for imaging of the as-deposited top surface. The statistical software package Minitab 17 was used for the generation of experiment design and their analysis.

3. Results and discussion

3.1 Normalized process map

Figure 5 shows a normalised process map, including works of previous researchers and our own trials. As described by Thomas et al. [14], we set the y-axis as $\frac{1}{h^*} = \frac{r_b}{h}$ and the x-axis as $\frac{q^*}{v^* l^*} = \frac{nQ}{2vlr_b\rho C_p(T_m-T_o)}$, which gives $x \cdot y$ as $E_o^* = \frac{nQr_b/v}{2r_b lh\rho C_p(T_m-T_o)}$. Note that by using these reduced variables, the process map should be independent from machine and material used. Here, normalized energy input, E_o^*, is essentially the ratio of energy absorbed by the material to that required for melting the volume $l \cdot h \cdot r_b$ [14]. The processability window of Ti-6Al-4V titanium alloy for producing components with a relative density greater than 99.95% is shown based on electron beam powder bed additive manufacturing (EBM) experiments [31]. Parameters used for SLM processing of the same material were found to be within these limits [32]. Similarly, for stainless steel processing by SLM, a lower limit of energy input, below which the relative density of the components produced was less than 99%, was established [33] and is shown in the figure. Work on SLM processing of tungsten is also shown [4,8]. Zhou et al. [4] achieved a maximum relative density of just 82.9%, indicating too low an energy input. On the other hand, Wang et al. [8] were able to achieve relative densities as high as 96% by increasing the energy input. Their results also show a wider processing window for high laser powers. Faidel et al. used a machine equipped with a 200 W laser for SLM manufacturing of molybdenum; they achieved a maximum relative density of just 82.5% [13]. In a another study, Wang et al. were able to achieve a relative density of 99.1% in SLM produced molybdenum using a 400 W laser [5]. Their work cannot been shown in the figure below as they did not provide enough information about the parameters used, only mentioning the line energy densities.

We selected the process parameters for our own trials 1-3 such that the normalized energy input is within the limits used by Faidel [13] and Wang [8].

3.2 Heat transfer modelling

Let us now assume a homogeneous static laser source with an infinite diameter shining perpendicularly on a powder bed for a given time. The 1D model (Eq. 5 and Eq. 6) is used to calculate the time-temperature profiles at different depths below the surface under such conditions. This is then used to predict the depth of a melt pool generated by the laser. Figure 7 shows the resultant time-temperature profile for $t_e = 100$ μs and $R_m = 45$ μm. The temperatures are plotted for a point at the surface, and points $d/2$, d and 45 μm below the surface. Where d is the depth of the melt pool at time $t = t_e$. Note that the maximum depth of the melt pool is not necessarily reached at the time of laser shutoff for the same reasons as discussed above. The time for the point 45 μm below the surface to reach the melting temperature increases as α decreases. For tungsten and molybdenum, with relatively high α, the maximum melt pool depth is achieved approximately at t_e. On the other hand, for stainless steel and titanium alloys with low α, 2.5 and 3 s longer, respectively, are required to reach the maximum melt pool depth. For both W and Mo, the time available for molten metal to flow before it is solidified, i.e. the time for which $T > T_m$, is significantly smaller than that for low conductivity materials. This might promote balling in W and Mo. It should also be noted that, in case of stainless steel and titanium alloys, a part of the melt pool exceeds the boiling temperature. While the extent of this vaporization is probably overestimated by the current model, boiling actually takes place in SLM

processing of some materials and leads, via the vapour recoil pressure, to the formation of a keyhole and possibly to the related porosity.

The two models described above predict vastly different energy inputs required for achieving the same melt pool depth (Figure 8). Therefore, the selection of the suitable analytical model is critical to arrive at sensible process parameters for experiments. For all materials, the Rosenthal model requires a higher energy input. The difference in energy input predicted by the two models increases with α. Unlike the Rosenthal solution, the 1D model assumes heat flow only along the z axis. This approach ignores any heat loss along any other direction, thus requiring a lower energy input for the generation of the same melt pool depth. Since this energy loss is directly proportional to α, the difference in energy input predicted by the models is directly proportional to it.

To find out the model more suitable for use with molybdenum, we check the validity criteria for these models, as discussed in section 2.2. r_o for molybdenum is calculated as $147 \ \mu m$ and $180 \ \mu m$ respectively for $t_e = 100 \ \mu s$ and $150 \ \mu s$. Since in our case, $r_b = 25 \ \mu m$ and p varies in the range of 25 to 55 μm, r_0 violates the validity condition for the 1D model ($r_b \gg r_o$). However, it meets the condition for the Rosenthal solution ($r_b \ll r_o$ and $p \ll r_o$). Therefore, for the given material and range of operating parameters, the Rosenthal solution for a moving point-size heat source is more accurate for use with our pulsed laser system than a model for a static heat source assuming one dimensional heat flow. This is somewhat surprising, because the 1D model was specifically developed for pulsed-laser systems. However, its underlying assumptions are violated in this particular case.

To further bolster this claim, a single-track experiment was performed. The experiment was carried out using = 190 W, $t_e = 150$ μs, and $p = 55$ μm. This gives an E_o^* of 12.6 (assuming $l = 30$ μm and $h = p$), being within the range used by Faidel [13]. For these parameters, the melt pool width predicted by the Rosenthal model is 38 μm and by 1D model is 290 μm (calculated from the melt pool depth, assuming a hemispherical shape). In our experiment, we measure a melt pool width of ~42 μm (cf. Figure 9), so our usage of the Rosenthal solution appears justified.

Based on the discussion above, the Rosenthal solution is used to set the range of parameters i.e. t_e, h, and p for further experimental work. We kept the process parameters such as to stay within the limits of E_o^* used in earlier works. The melt pool depth, R_m was calculated and was used to obtain the value for d^*. d^* acts as the basic selection criterion for experiments.

3.3 Further process parameter optimization via bulk specimen experiments

Molybdenum is susceptible to balling and cracks from thermal residual stress, therefore, requiring additional parameter optimization. Since balling is dependent on the solidification conditions [8,34], in particular on the ability of the molten material to flow and wet the underlying material, we first attempt to separate the behaviour of a single melt pool from the optimization of melt pool overlaps. We achieve this by setting $d^* = 0$, i.e. ensuring a minimum melt pool overlap or interaction. The parameter to be optimized in the first set of experiments, trial 1, is the interaction time, t_e, since (next to the laser power, that was kept constant at its maximum value), it has the most direct influence on the melt pool existence time and melt superheat. In the experiment, we varied t_e between 100 and 200 μs. We repeated the experiment for three different values of the hatch spacing (45, 50 and 55 μm), each large enough to keep $d^* = 0$. $p, l,$ and Q were set as 50 μm, 30 μm, and 143 W respectively (i.e. p was chosen as twice the beam radius, l was chosen as the lowest reasonable value for the used powder and Q was set as the maximum power output of the machine at the time of experiment). The resulting porosity as a function of t_e (Figure 10) shows that there is an optimum value of $t_e = 150$ μs. In the next step, we aim to optimize the process parameters for reducing residual thermal stress. Stress is largely influenced by the scan parameters, i.e. hatch spacing, h, and point distance, p. Initial experiments conducted with values chosen such that $d^* \geq 1$ (not shown here) yielded porosities that

did not depend on p and h in a systematic manner. We therefore conducted the next set of experiments, trial 2, keeping $0 \leq d^* < 1$, using the same layer thickness and laser power as trial 1 and keeping the optimized $t_e = 150$ µs constant. h and p were varied between 35 to 55 µm and 25 to 45 µm respectively. We used a contour plot based on response surface analysis [35] to find an optimal process window (Figure 11). Surprisingly, intermediate values for p and h (intermediate d^*) lead to the lowest porosity values and not values that lead to a large melt pool overlap (maximum d^*).

To understand the counterintuitive results from trial 2, we performed additional single track experiments. For $p = 25$ µm, cracks running through the track were observed; the cracks were eliminated on increasing p to 35 µm (Figure 12). This is attributed to the presence of higher residual stresses resulting in cracking when the consecutive melt pools are too close to each other. These cracks appear as additional porosity in our density measurements.

With interaction time, t_e, hatch spacing, h, and point distance, p, optimized for reduced balling and residual thermal stresses, we vary the remaining parameters, layer thickness, l, and laser power, Q, to achieve $d^* > 1$. p and h were set as 35 and 45 µm respectively from within the process window in the contour plot above. A significant reduction in porosity was observed upon increasing the laser power to 190 W and decreasing layer height to 20 µm in this third trial (see Figure 13).

Our extended approach to parameter selection as detailed in this section is summarized in the flowchart in Figure 14.

Examining the top surface of the samples from trial 2 and trial 3 (Figure 15) revealed that the balling phenomenon was still taking place during the process. Since previous studies [1,4] suggested that remelting scans can be used to limit balling, we introduced a remelting scan after each layer. For this scan, we used the same process parameters as before, but a focus offset of 4. A marked improvement in the roughness of the top surface is observed (compare Figure 16 a) to Figure 15). This is also correlated with the reduction in porosity (Figure 16.b). Finally a relative density of 97.4% is achieved. Multiple cracks can still be observed in the top surface, probably as a result of thermal residual stresses. Increasing the base plate temperature might help in reducing them, however, this remedy was outside the scope of this work.

3.4 SLM manufacturing of Aluminium

To further demonstrate the strength of our predictive approach over the conventional energy density based approach [5,12,13], we briefly present some of the results from an ongoing work on Al-0.44wt% Sc alloy. We made a total of eight samples using a continuous laser system, three each with energy densities [12] of 139 and 174 J/mm³ and two with 208 J/mm³. We vary the laser velocity between 300 and 900 mm/s while adjusting laser power to reach the desired energy density. Note that the eight samples are shown by only three points, each representing a different energy density, in the normalized process map (Figure 5). Figure 17 shows the measured relative density with respect to the calculated melt pool depth, R_m, using the Rosenthal equation and Figure 18 shows two exemplary micrographs. The corresponding d^* values are plotted along the secondary y-axis. Detailed experimental conditions for these results are given in the supplementary information. Despite keeping the energy density constant, and identical coordinates in Figure 5, large variations in relative density are observed (cf. Figure 18). Increasing the energy density does help in improving relative density even for the same R_m, i.e. the curves don't completely overlap as would be expected for a perfect prediction of the melt pool behaviour. However, relative densities above 98% are observed only for $d^* > 1$, which is in agreement with our heuristic.

4. **Discussion**

From the normalized process map, shown in Figure 5, it is clear that there is a minimum value of the energy that must be supplied to produce high-density components. The usual approach to finding this minimum energy for different materials has been mostly experimental. We further show that two experiments with identical coordinates in Figure 5 can lead to very different experimental outcomes in terms of porosity (see e.g. Figure 18). This limits the use of normalized process maps, although an improvement over volumetric energy density, to identify the minimum energy requirement.

In this study, we establish an analytical parameter, d^*, as the ratio of the minimum overlap between two neighbouring melt pools to the layer thickness. To produce completely dense components, d^* should be greater than or equal to 1. This criterion can be used to identify the minimum energy input requirements, potentially replacing time-consuming and expensive experimental studies.

The minimum overlap thickness can be easily worked out based on the scan parameters, for example, p and h in a pulsed-laser system, once the melt pool radius (R_m) is known. In this study, we suggest the use of analytical heat transfer modelling to predict R_m. When selecting a particular analytical solution of the heat transfer differential equation, it is important to check the validity of the underlying assumptions used to derive this solution. This has been illustrated in Figure 8. At this stage it is important to point out that neither of our analytical models are valid for stainless steel and titanium alloys, as the distance heat can travel during the interaction time, r_o, in these cases, is in the same range as the beam radius, r_b. We are currently developing analytical models that will be applicable to these materials.

In case of the refractory metals, heat diffusion through the material is fast, leading to faster cooling. We show that we can use the Rosenthal solution to model the melt pool depth (Figure 6). However, a sufficient energy input via the laser beam and hence a minimum overlap of melt pools is not the only criterion to reach low porosity. The high thermal conductivity of refractory metals means that there is little time for the molten metal to flow before it solidifies. Therefore, the probability of the metal solidifying before it wets the previous layer or substrate is very high. This results in pronounced balling in these materials. Further, because of high thermal conductivity, high thermal gradients are generated during the SLM process. These strong thermal gradients generate strong local strains owing to thermal expansion of the material. On cooling down to the room temperature, they remain in the material as residual stresses, causing cracking. This is particularly true for refractory metals which are brittle in nature. Therefore, steps to reduce thermal residual stress and balling need to be taken during additive manufacturing of refractory metals.

In this work, we present a heuristic that can be followed when developing additive manufacturing process parameters for new materials. First, a wide processability window for a given material is worked out using normalized process maps. This is then further optimized based on analytical heat transfer modelling. Lastly, a suitable operating window is identified by performing experiments based on DOE concepts. We expect that the use of such a framework lowers the number of experiments that are required in process development studies. A proof of this is, however, difficult to achieve because the number of experiment required in a trial-and-error approach is by definition a random variable and a user could obtain good results quickly either by luck or by intuition. Therefore, perhaps the most valuable contribution of our approach is that it gives a clear optimization heuristic instead of requiring either many trials, luck, or intuition.

The thermal modelling approach used in this study is easy to implement and can be performed on any personal computer using standard mathematical software, for example, Matlab®. The effectiveness of the dimensionless parameter d^* introduced by us over the currently used energy density is best illustrated by the experiments on an Al-Sc alloy in Figure 17: Large variations in relative density were observed even when using the same energy density. Our predictions, however, that d^* values greater than 1 lead to high relative densities (>98% in this case) turned out to be correct.

Note that using this heuristic, we were able to obtain a relative density of 97.4% for the SLM production of molybdenum using only a 200W laser. Previous works were limited to 82.5% for the same maximum laser power [13], and only achieved a relative density higher than in our study, 99.1 %, by using a 400W laser [5].

Our method has the potential to be expanded beyond simply optimizing processing parameters for maximum density. Once the temperature field is known, quantities like thermal gradients and cooling rates can easily be calculated that govern the solidification and hence the microstructure evolution. Thus, we envision the optimization of not only porosity, but also other target features such as a certain microstructures leading to improved mechanical properties.

5. Conclusions

- Analytical models can be used to predict the melt pool shape and size. From these predictions, the overlap of melt pools can be calculated.
- We define a dimensionless melt pool overlap depth, d^*. To manufacture components with high density, d^* should be greater than or equal to 1.
- We demonstrate a heuristic to predict SLM process parameters. It involves an initial identification of a processing window through normalized process maps and further parameter optimization based on analytical heat transfer models and DOE based experiments.
- For SLM processing of molybdenum, additional optimization of process parameters to reduce balling and thermal residual stresses is required.
- Using our parameter optimization approach, we achieve a relative density of more than 97% during SLM processing of Molybdenum using a 200 W laser and a relative density of 99.7% for SLM produced Al-0.44wt% Sc alloy.
- We envision that the thermal modelling approach can be further extended to predict microstructures in SLM-produced parts.

6. Acknowledgments

References

[1] C.Y. Yap, C.K. Chua, Z.L. Dong, Z.H. Liu, D.Q. Zhang, L.E. Loh, S.L. Sing, Review of selective laser melting: Materials and applications, Appl. Phys. Rev. 2 (2015) 41101. doi:10.1063/1.4935926.

[2] A.B. Spierings, M. Schneider, R. Eggenberger, Comparison of density measurement techniques for additive manufactured metallic parts, Rapid Prototyp. J. 17 (2011) 380–386. doi:10.1108/13552541111156504.

[3] B. Vrancken, L. Thijs, J.-P. Kruth, J. Van Humbeeck, Microstructure and mechanical properties of a novel β titanium metallic composite by selective laser melting, Acta Mater. 68 (2014) 150–158. doi:10.1016/j.actamat.2014.01.018.

[4] X. Zhou, X. Liu, D. Zhang, Z. Shen, W. Liu, Balling phenomena in selective laser melted tungsten, J. Mater. Process. Technol. 222 (2015) 33–42. doi:10.1016/j.jmatprotec.2015.02.032.

[5] D. Wang, C. Yu, J. Ma, W. Liu, Z. Shen, Densification and crack suppression in selective laser melting of pure molybdenum, (2017). doi:10.1016/j.matdes.2017.04.094.

[6] K. Kempen, L. Thijs, J. Van Humbeeck, J.-P. Kruth, Materials Science and Technology Processing AlSi10Mg by selective laser melting: parameter optimisation and material characterisation Processing AlSi10Mg by selective laser melting: parameter optimisation and material characterisation, (2017). doi:10.1179/1743284714Y.0000000702doi.org/10.1179/1743284714Y.0000000702.

[7] P. Mercelis, J.-P. Kruth, S.R. Pogson, P. Fox, C.J. Sutcliffe, W.O.' Neill, Rapid Prototyping Journal The production of copper parts using DMLR, Rapid Prototyp. J. Iss Rapid Prototyp. J. Iss Rapid Prototyp. J. Iss Assem. Autom. 9 (2003) 334–343. http://dx.doi.org/10.1108/13552540310502239.

[8] D. Wang, C. Yu, X. Zhou, J. Ma, W. Liu, Z. Shen, Dense Pure Tungsten Fabricated by Selective Laser Melting, Appl. Sci. 7 (2017) 430. doi:10.3390/app7040430.

[9] Y. Guo, L. Jia, B. Kong, N. Wang, H. Zhang, Single track and single layer formation in selective laser melting of niobium solid solution alloy, (2017). doi:10.1016/j.cja.2017.08.019.

[10] N.K. Tolochko, S.E. Mozzharov, I.A. Yadroitsev, T. Laoui, L. Froyen, V.I. Titov, M.B. Ignatiev, P. Mercelis, J.-P. Kruth, Rapid Prototyping Journal Balling processes during selective laser treatment of powders"Balling processes during selective laser treatment of powders Balling processes during selective laser treatment of powders, Rapid Prototyp. J. Rapid Prototyp. J. Rapid Prototyp. J. Iss Assem. Autom. 10 (2004) 78–87. http://dx.doi.org/10.1108/13552540410526953.

[11] J.O. Milewski, Additive Manufacturing of Metals, Springer International Publishing, Cham, 2017. doi:10.1007/978-3-319-58205-4.

[12] R. Li, M. Wang, T. Yuan, B. Song, C. Chen, K. Zhou, P. Cao, Selective laser melting of a novel Sc and Zr modified Al-6.2 Mg alloy: Processing, microstructure, and properties, (2017). doi:10.1016/j.powtec.2017.06.050.

[13] D. Faidel, D. Jonas, G. Natour, W. Behr, Investigation of the selective laser melting process with molybdenum powder, Addit. Manuf. 8 (2015) 88–94. doi:10.1016/j.addma.2015.09.002.

[14] M. Thomas, G.J. Baxter, I. Todd, Normalised model-based processing diagrams for additive layer manufacture of engineering alloys, Acta Mater. 108 (2016) 26–35. doi:10.1016/j.actamat.2016.02.025.

[15] J.C. Ion, H.R. Shercliff, M.F. Ashby, Diagrams for laser materials processing, Acta Metall. Mater. 40 (1992) 1539–1551. doi:10.1016/0956-7151(92)90097-X.

[16] A. Foroozmehr, M. Badrossamay, E. Foroozmehr, S. Golabi, Finite Element Simulation of Selective Laser Melting process considering Optical Penetration Depth of laser in powder bed, Mater. Des. 89 (2016) 255–263. doi:10.1016/j.matdes.2015.10.002.

[17] T. Heeling, M. Cloots, K. Wegener, Melt pool simulation for the evaluation of process parameters in selective laser melting, Addit. Manuf. 14 (2017) 116–125. doi:10.1016/j.addma.2017.02.003.

[18] L.E. Criales, Y.M. Arısoy, T. Özel, A Sensitivity Analysis Study on the Material Properties and Process Parameters for Selective Laser Melting Of Inconel 625, in: ASME 2015 Int. Manuf. Sci. Eng. Conf. MSEC2015, Charlotte, North Carolina, USA, 2015: pp. 1–10.

11

[19] E.M. Breinan, B.H. Kear, Rapid solidification laser processing, in: M. Bass (Ed.), Laser Mater. Process., North-Holland publishing company, New York, 1983: pp. 235–296.

[20] K. Zeng, D. Pal, B. Stucker, A review of thermal analysis methods in Laser Sintering and Selective Laser Melting, in: Solid Free. Fabr. Symp., Austin, Texas, USA, 2012: pp. 796–814.

[21] D. Dye, O. Hunziker, R.C. Reed, Numerical analysis of the weldability of superalloys, Acta Mater. 49 (2001) 683–697. doi:10.1016/S1359-6454(00)00361-X.

[22] D. Rosenthal, The Theory of Moving Sources of Heat and Its Application to Metal Treatments, Trans. ASME. 43 (1946) 849–866.

[23] J.H. Bechtel, Heating of solid targets with laser pulses, J. Appl. Phys. 46 (1975) 1585–1593. doi:10.1063/1.321760.

[24] J.F. Ready, Effects of High-Power Laser Radiation, Academic Press Inc., New York, 1971.

[25] K. Brugger, Exact Solutions for the Temperature Rise in a Laser- Heated Slab, J. Appl. Phys. 43 (1972) 577–583. doi:10.1063/1.1661159.

[26] M.A. Bramson, Infrared Radiation, Springer US, Boston, MA, 1968. doi:10.1007/978-1-4757-0911-7.

[27] R. Deffley, Development of Processing Strategies for the Additive Layer Manufacture of Aerospace Components in Inconel 718, University of Sheffield, 2012.

[28] C.D. Boley, S.A. Khairallah, A.M. Rubenchik, Calculation of laser absorption by metal powders in additive manufacturing, Appl. Opt. 54 (2015) 2477. doi:10.1364/AO.54.002477.

[29] M.N. Ozisik, Heat Conduction, 2nd ed., John Wiley & Sons Inc., New York, 1993. doi:10.1002/9781118411285.

[30] H.S. Carslaw, J.C. Jaeger, Conduction of Heat in Solids, 2nd ed., Oxford U.P., London, 1959.

[31] V. Juechter, T. Scharowsky, R.F. Singer, C. Körner, Processing window and evaporation phenomena for Ti–6Al–4V produced by selective electron beam melting, Acta Mater. 76 (2014) 252–258. doi:10.1016/j.actamat.2014.05.037.

[32] M. Simonelli, C. Tuck, N.T. Aboulkhair, I. Maskery, I. Ashcroft, R.D. Wildman, R. Hague, A Study on the Laser Spatter and the Oxidation Reactions During Selective Laser Melting of 316L Stainless Steel, Al-Si10-Mg, and Ti-6Al-4V, Metall. Mater. Trans. A. 46 (2015) 3842–3851. doi:10.1007/s11661-015-2882-8.

[33] C. Kamath, B. El-dasher, G.F. Gallegos, W.E. King, A. Sisto, Density of additively-manufactured, 316L SS parts using laser powder-bed fusion at powers up to 400 W, Int. J. Adv. Manuf. Technol. 74 (2014) 65–78. doi:10.1007/s00170-014-5954-9.

[34] A. Gusarov, I. Yadroitsev, P. Bertrand, I. Smurov, Heat transfer modelling and stability analysis of selective laser melting, (2007). doi:10.1016/j.apsusc.2007.08.074.

[35] Engineering Statistics Handbook, NIST/SEMATECH. (2012). http://www.itl.nist.gov/div898/handbook (accessed September 24, 2015).
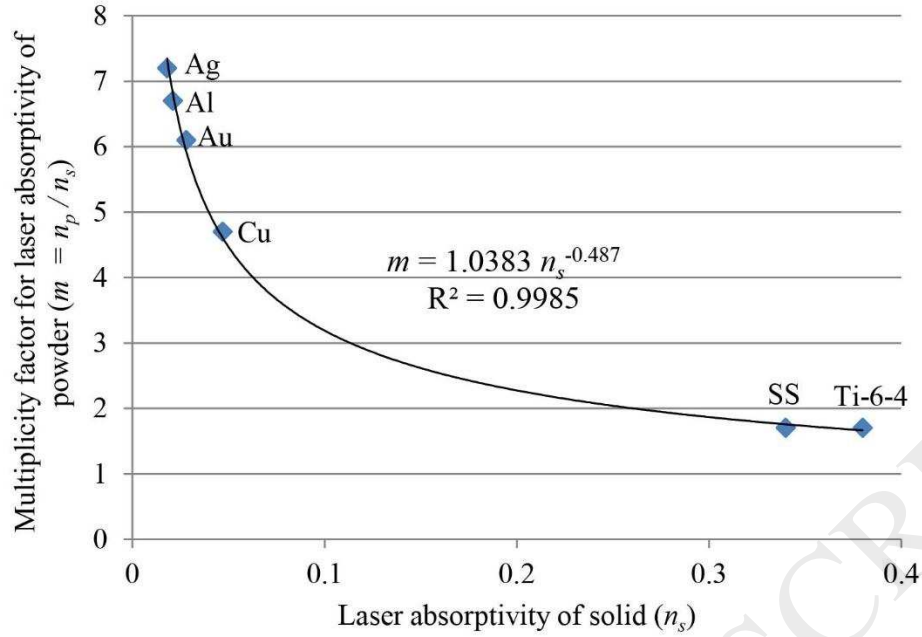
Figure 1: Regression analysis for multiplicity factor for laser absorptivity of powder (m) with respect to laser absorptivity for solid (n_s), based on results from Boley et al. [28]
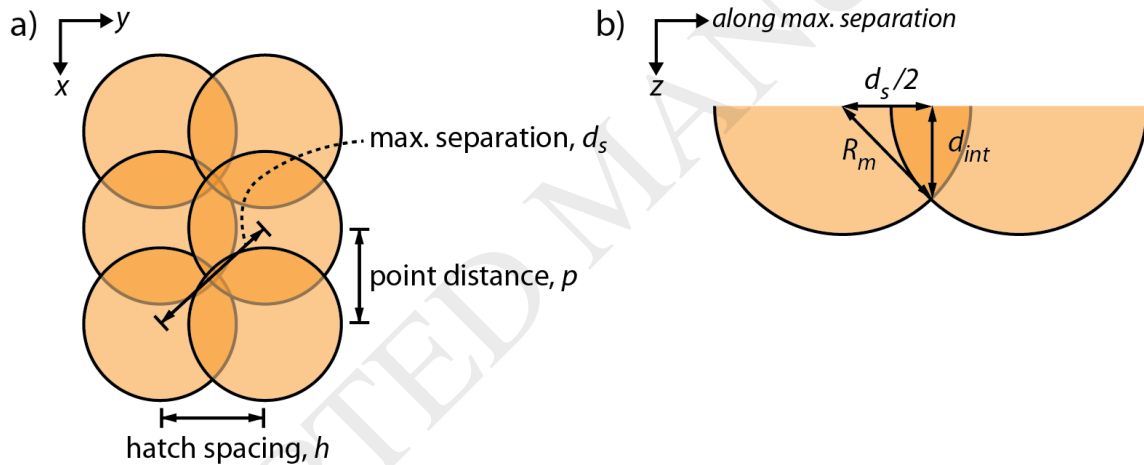

Figure 2: a) Top view of the build plane, showing maximum separation (d_s) between two overlapping melt pools within a same layer in a pulsed laser SLM system; for continuous laser $d_s = h$ b) Side view along d_s, showing minimum overlap depth (d_{int}) for the same melt pools. For complete overlap of the melt pools, d_{int} should be greater than the layer thickness (l) of the powder laid after each complete scan of the previous layer.

13
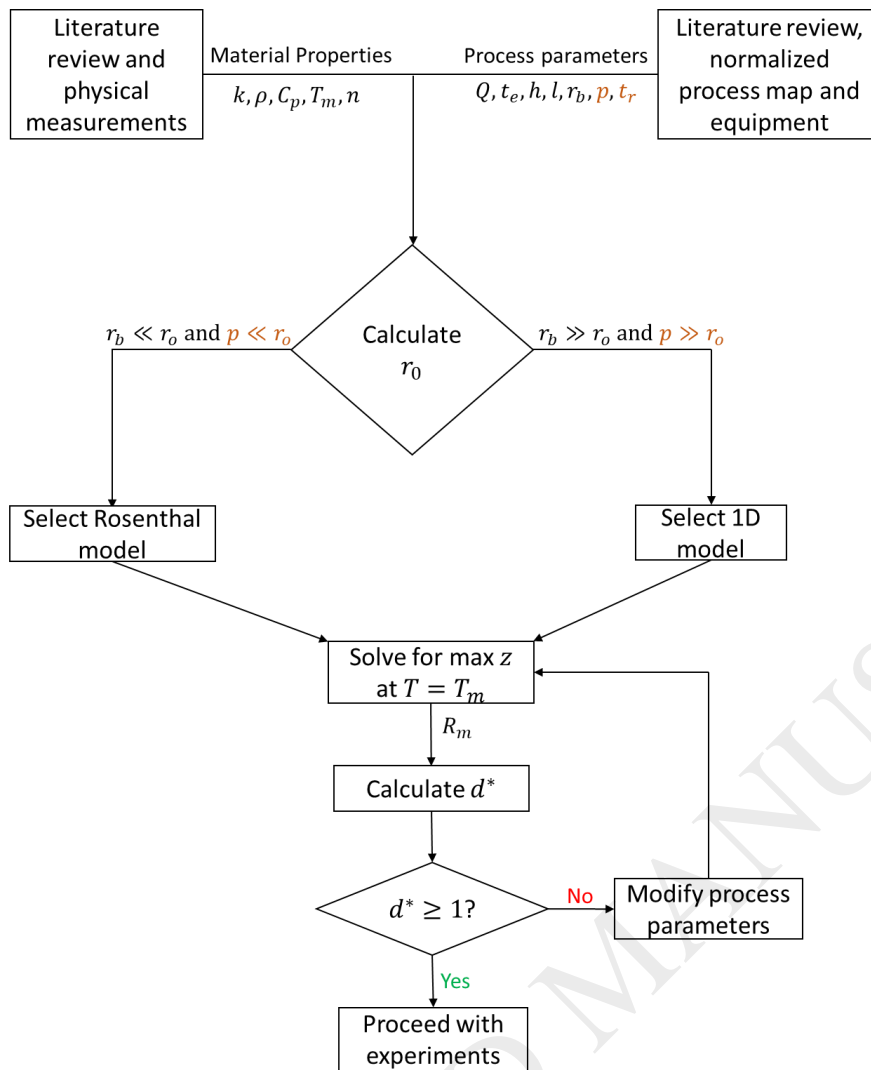
Figure 3: Flow chart depicting our proposed methodology for predictive process development. The parameters in orange are only required for pulsed laser system. For materials which are susceptive to failure from residual stresses or balling additional parameter optimization steps are required (see Figure 14).
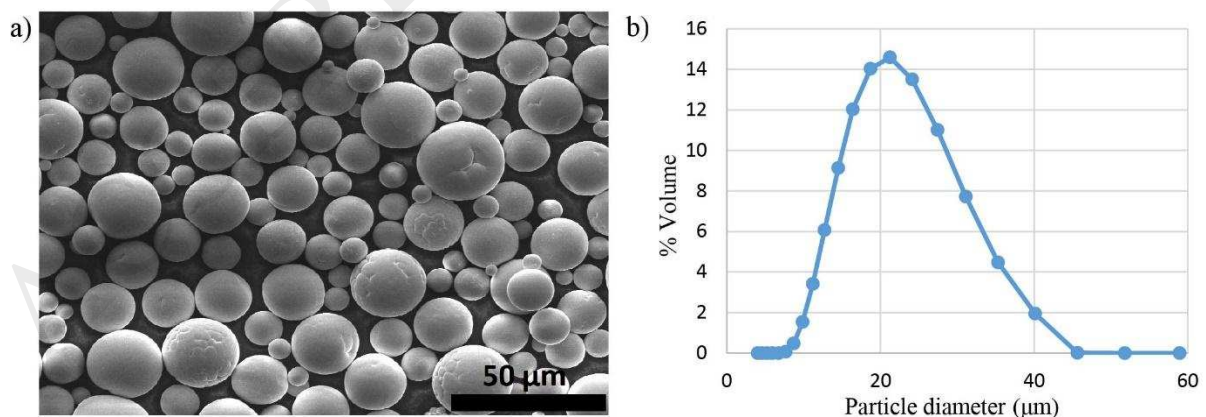
Figure 4: a) SEM (SE) image of the used powder b) Particle size distribution of the powder measured using laser diffraction. Measured particle size fractions are $d_{10} = 14$ μm, $d_{50} = 21.8$ μm and $d_{90} = 33.3$ μm
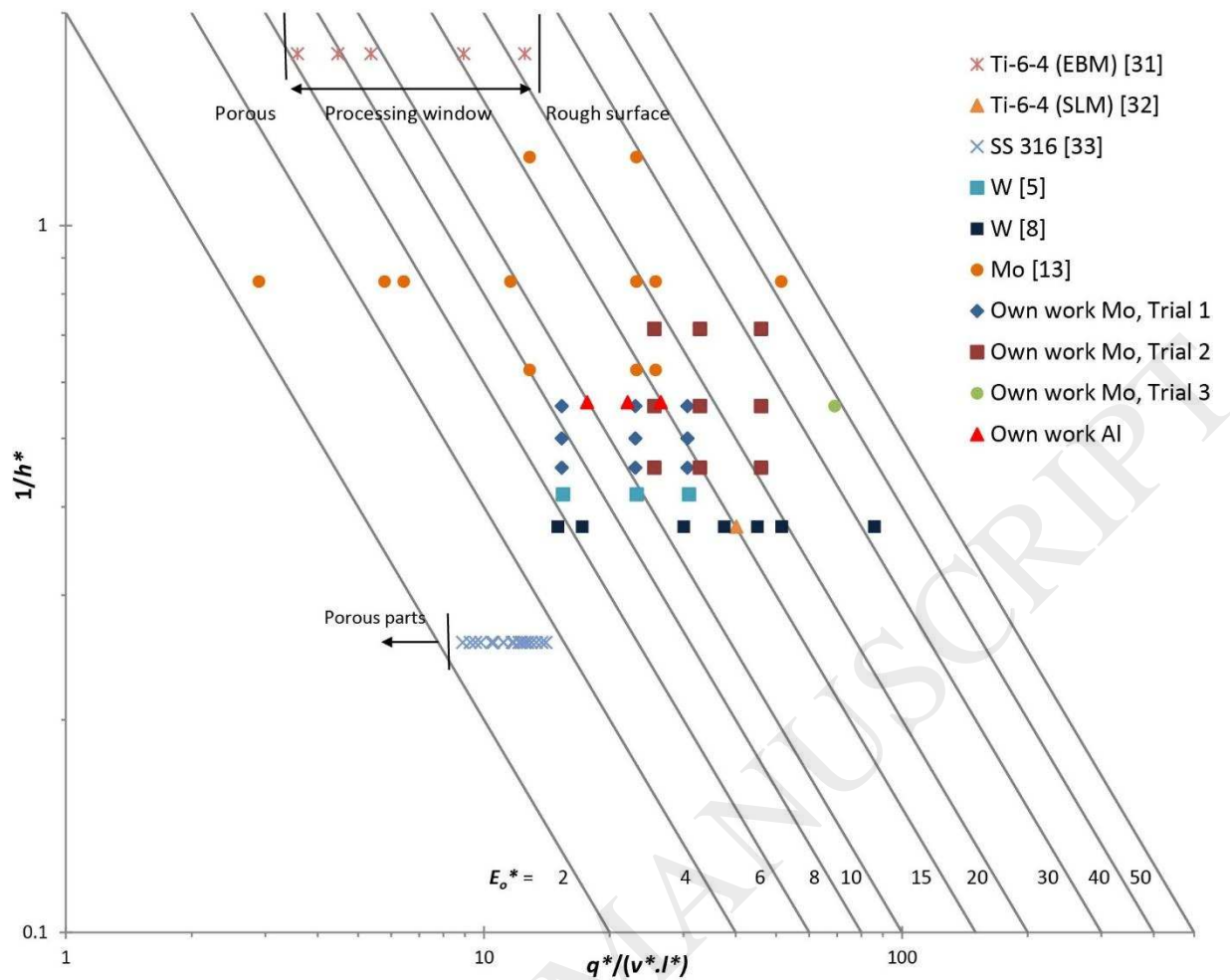
Figure 5: Normalized process map showing different works along with process window from the literature. Best relative densities of 99% and 99.5% were observed for stainless steel and titanium alloy respectively [31–33], whereas 96% for tungsten [8] and only 82.5% for Molybdenum [13]. Our own Molybdenum and Aluminium work is also shown.

15
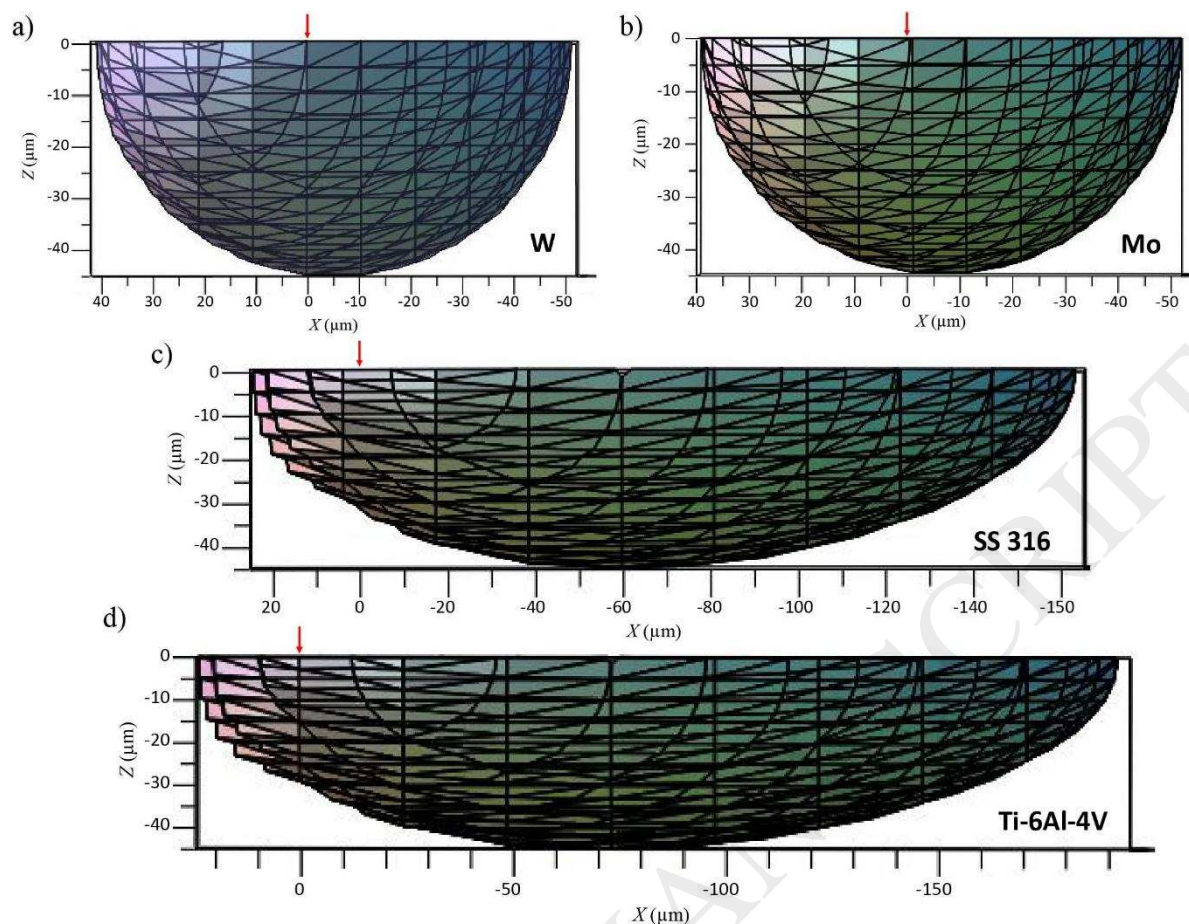
Figure 6: Melt pool geometries along x-z plane of a) Tungsten, b) Molybdenum, c) SS 316, and d) Ti-6Al-4V modelled based on the Rosenthal solution for moving point-size heat source. The point of laser incidence is indicated by red arrows in the figure. The melt pools have been plotted for laser velocity of 0.38 ms^{-1}. The power is adjusted so as to obtain the maximum melt pool depth of 45 μm for all cases. ($\alpha_W = 6.94 \times 10^{-5}$m^{2}s^{-1}, $\alpha_{Mo} = 5.41 \times 10^{-5}$m^{2}s^{-1}, $\alpha_{SS} = 3.69 \times 10^{-6}$m^{2}s^{-1}, $\alpha_{Ti} = 3.09 \times 10^{-6}$m^{2}s^{-1})

16
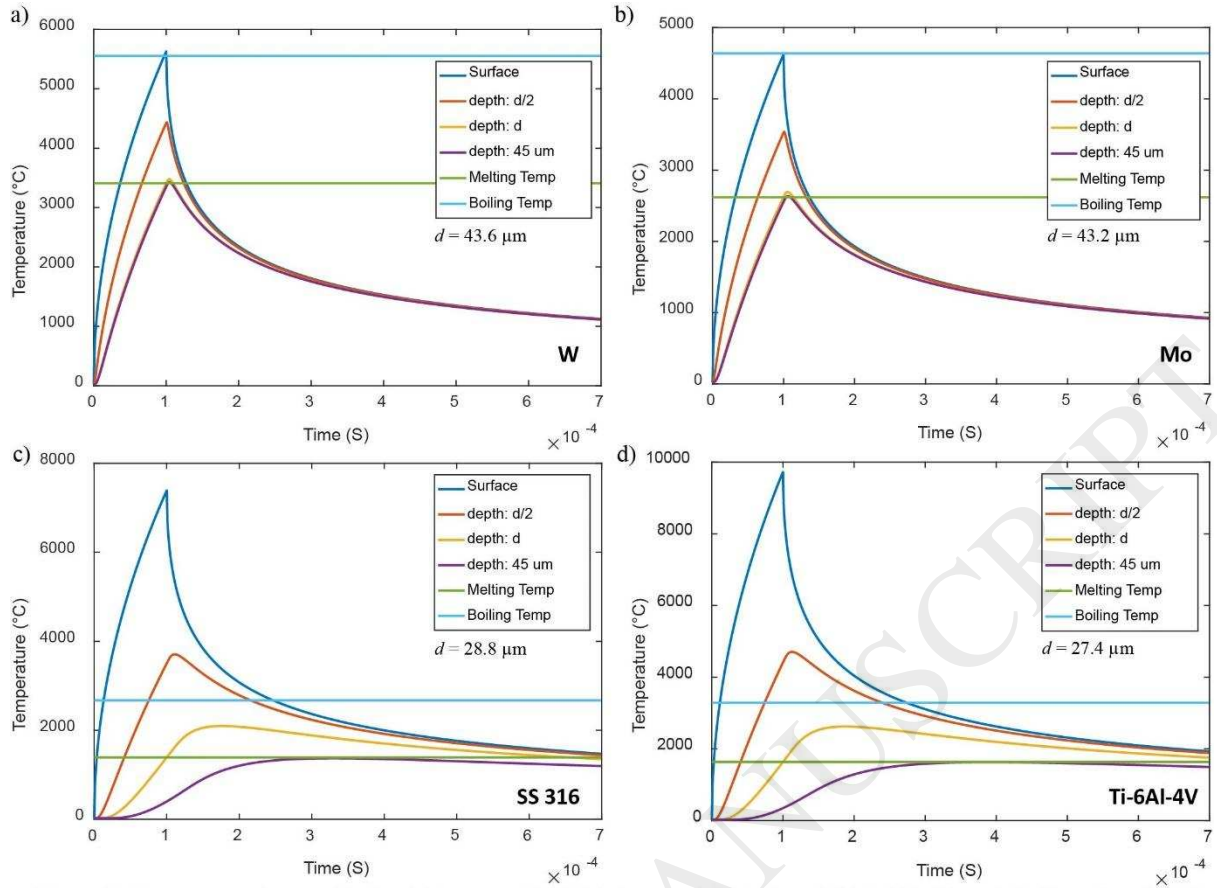
Figure 7: Temperature-time profile for a) Tungsten, b) Molybdenum, c) SS 316, and d) Ti-6Al-4V modelled based on the 1D model. Here d is the depth of the melt pool at time $t = t_e$. The profiles have been developed for $t_e = 100$ μs. The power was adjusted so as to obtain $R_m = 45$ μm for all cases.
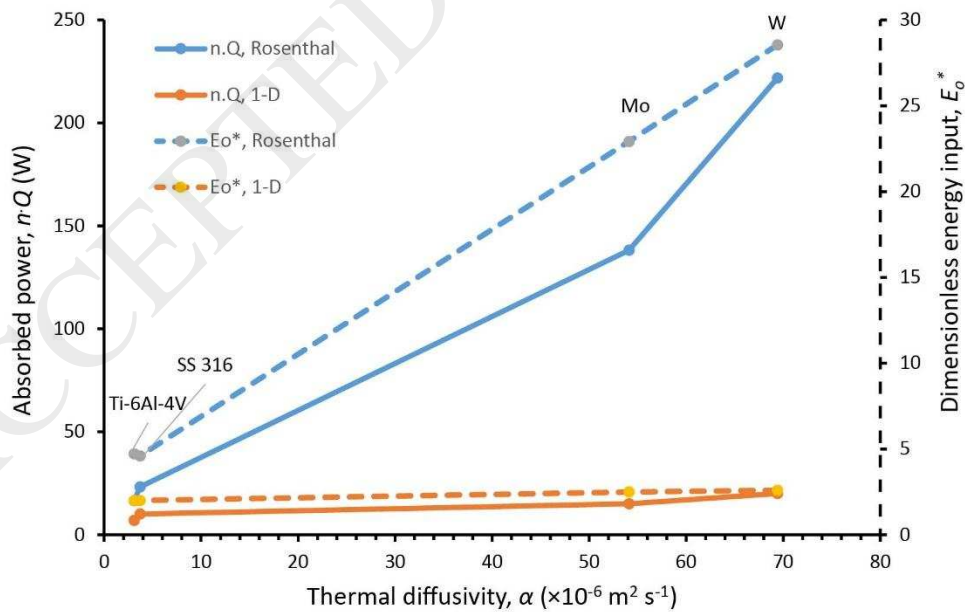
Figure 8: Absorbed power (solid line) and dimensionless energy input (dotted line) required for generating a melt pool depth of 45 μm as predicted by the Rosenthal solution and 1D model. The parameters used for these calculations are $h = 45$ μm, $= 45$ μm , $l = 30$ μm, $r_b = 25$ μm and $t_e = 100$ μs. Notice the difference between the two models arising out of their underlying assumptions.

Figure 9: Optical micrograph of the top surface of a single track. Process parameters: $Q = 190$ W, $t_e = 150$ µs, and $p = 55$ µm. Predicted melt pool radius (R_m) from Rosenthal solution is 38 µm and from 1D model is 290 µm, compared with 42 µm measured experimentally.
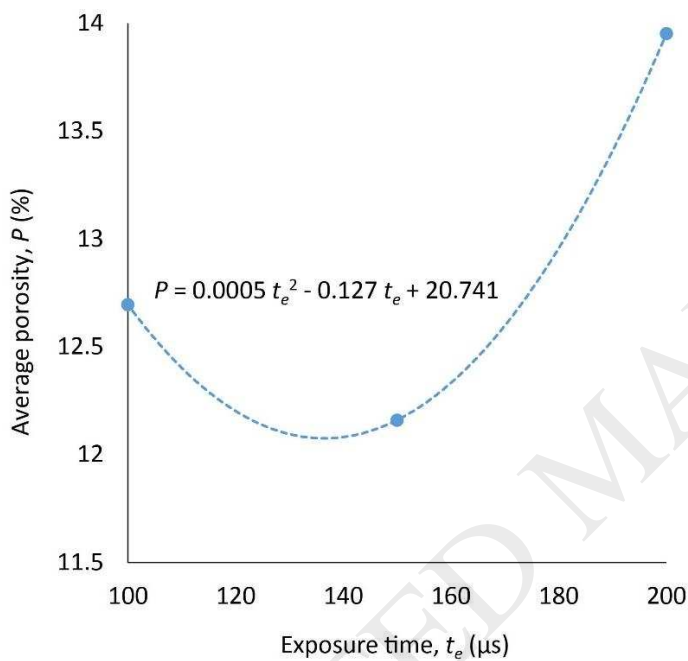

Figure 10: Main effects plot from statistical analysis of the experimental results for % porosity for trial 1, the corresponding regression equation is also shown. Based on this, the optimum value of t_e was determined as 150 µs.
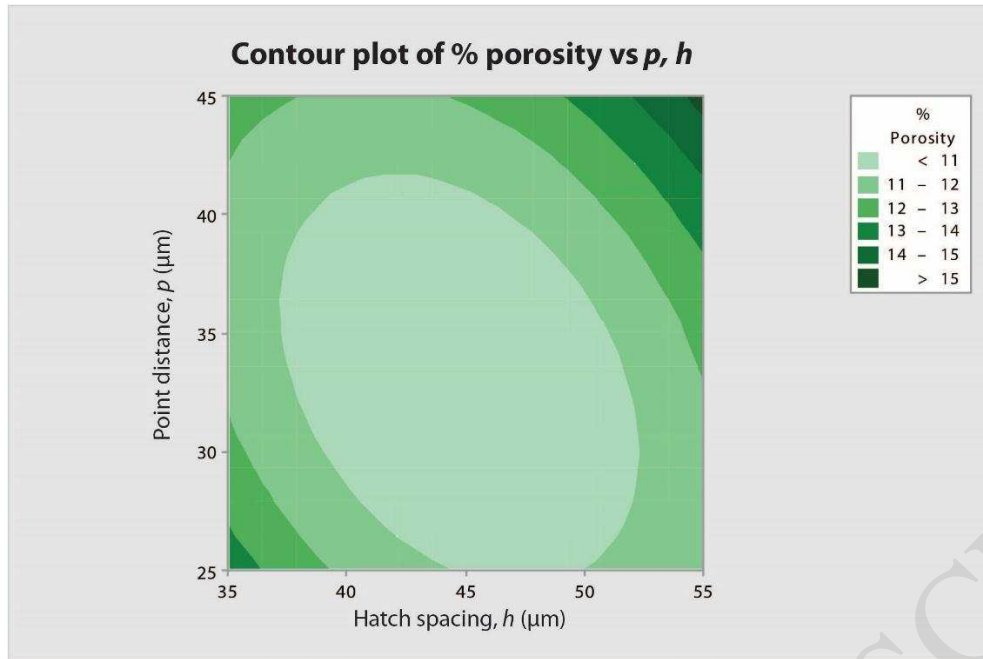
Figure 11: Contour plot of the response surface from statistical analysis of the experimental results for % porosity using Minitab software for trial 2.
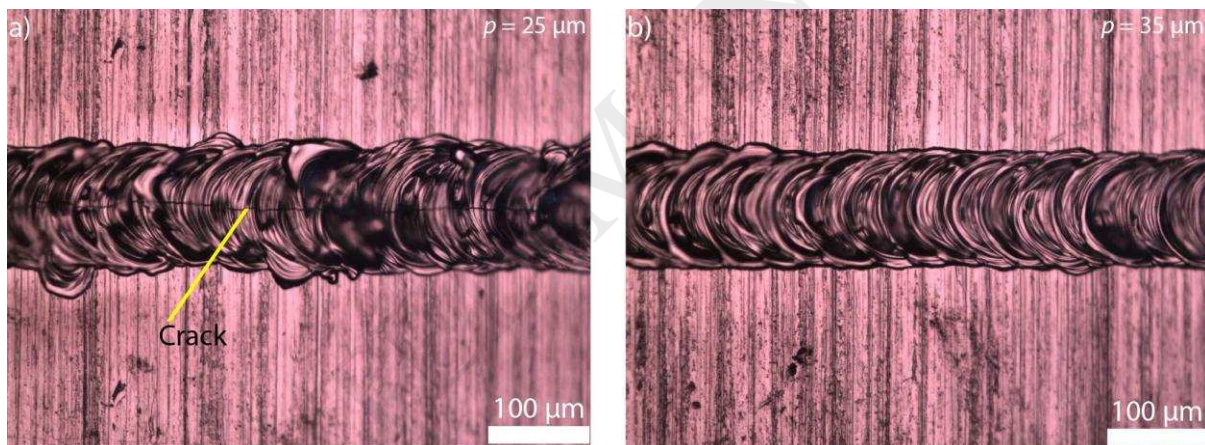

Figure 12: Optical micrograph of the top surface of a single track. Process parameters: $Q = 190\ W$, $t_e = 150\ \mu s$, and $p = 25\ \mu m$ in a) and $35\ \mu m$ in b). A crack can be observed at the centre of the track for smaller point distance. This is attributed to the presence of higher thermal residual stresses.
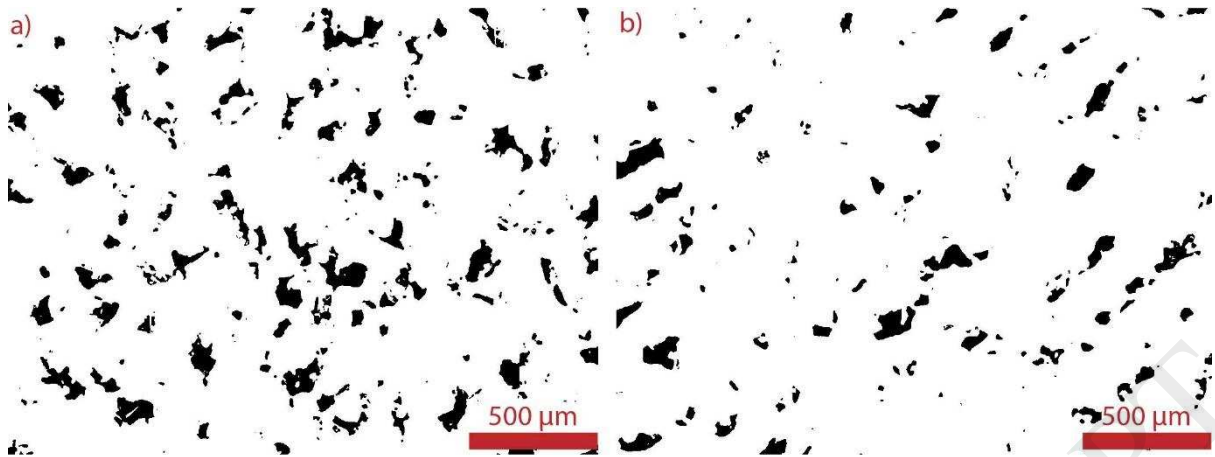
Figure 13: Optical micrograph (50×) of a plane normal to top surface of a) sample 2B2 ($Q = 143$ W, $l = 30$ μm) and b) trial 3 ($Q = 190$ W, $l = 20$ μm); $p = 35$ μm, $h = 45$ μm and $t_e = 150$ μs for both. Clear reduction in porosity can be observed. Mean measured area of porosities in a) is 9.7 % and in b) is 5.6 %
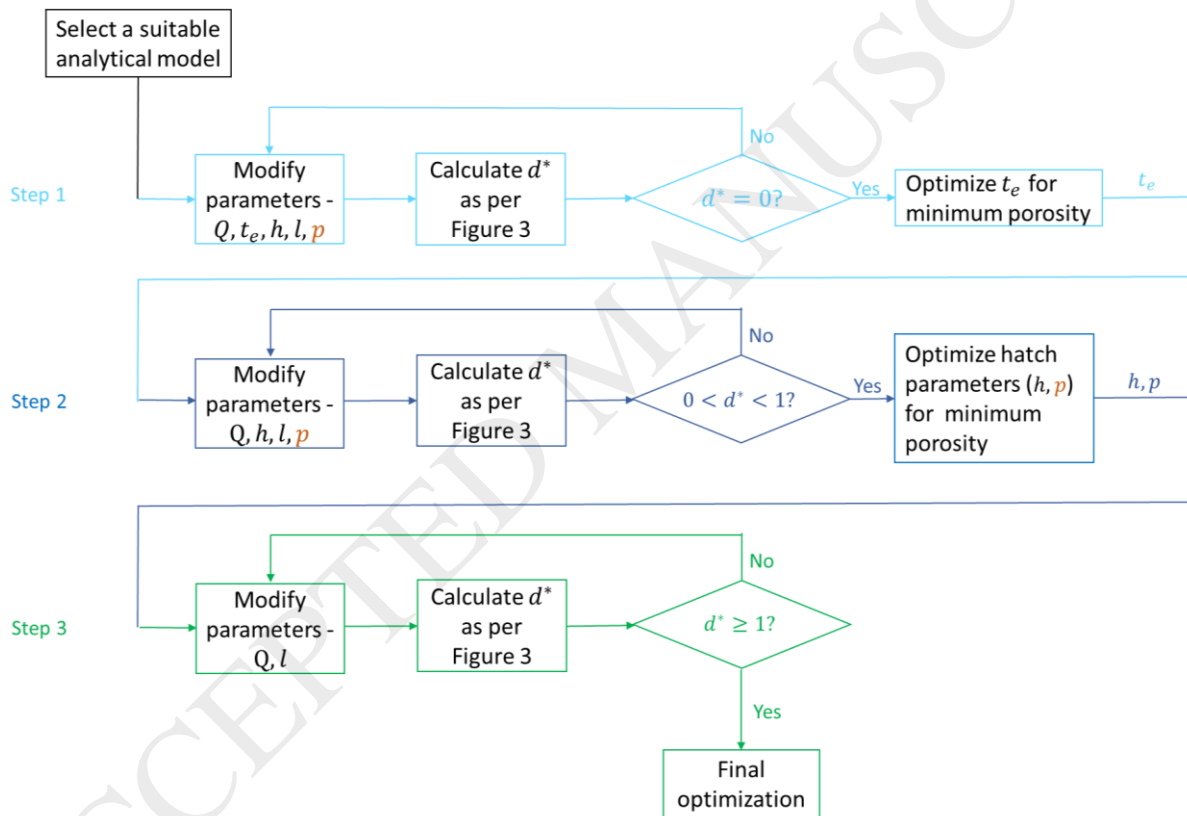

Figure 14: Schematic showing our predictive approach to process development including additional optimization steps, step 1 and step 2, for minimizing balling and cracking due to thermal residual stresses. The parameters in orange are only required for pulsed laser system.
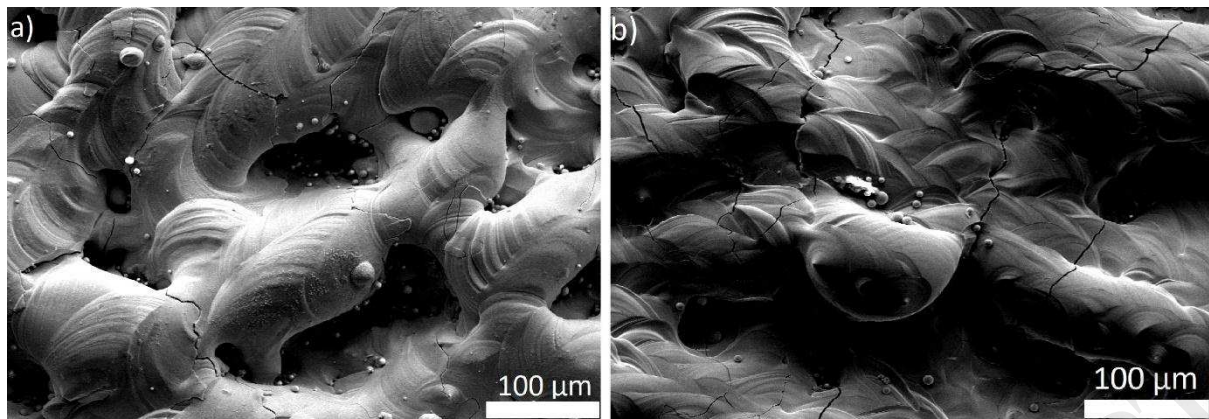
Figure 15: SEM images of the top surface of a) sample 2B2 and b) sample 3. Notice the roughness of the top surface of both specimens. This is attributed to a phenomenon known as balling [4]. Also note the presence of multiple cracks.
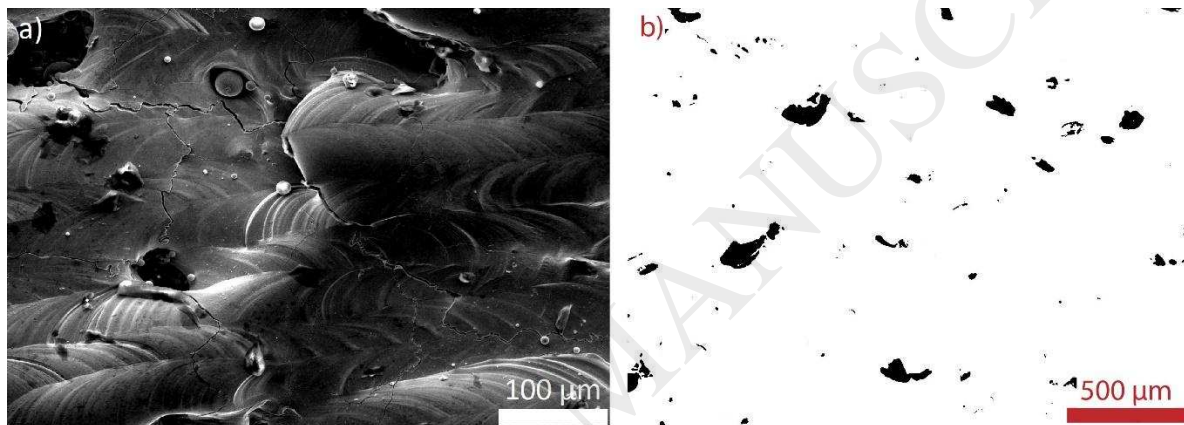

Figure 16: a) SEM image of the top surface and b) Optical micrograph of a plane normal to the top surface of sample with remelting scan (trial 4). Average porosity is 2.6%. Notice the improvement in surface roughness and reduction in porosity.
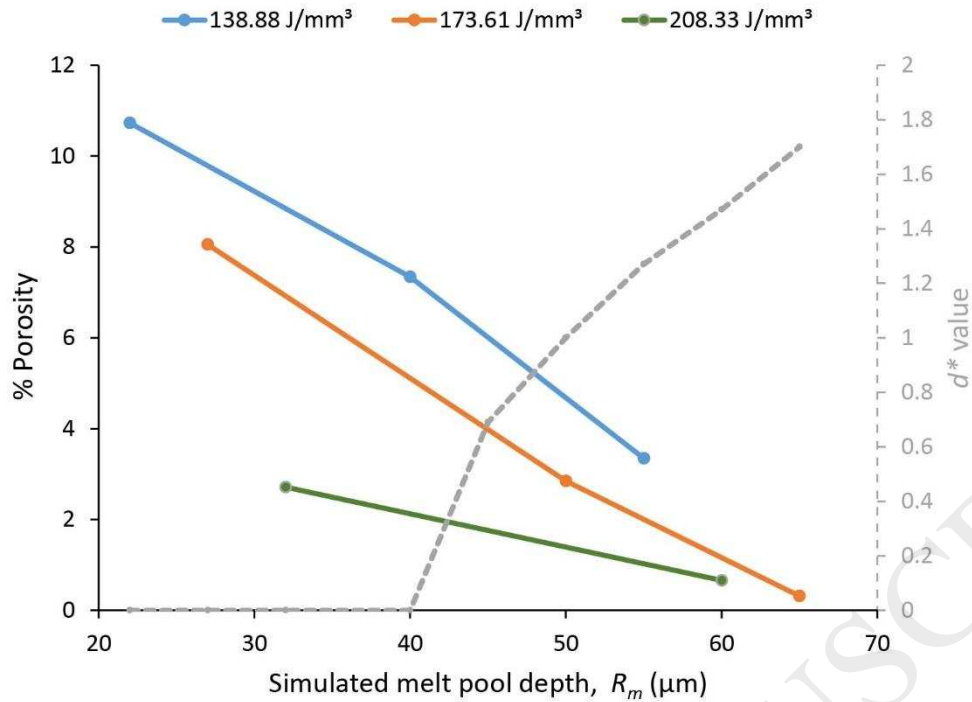
Figure 17: Plot showing measured % porosity with respect to R_m for samples produces with three different energy densities – 138.88, 173.61, 208.33 J/mm³. The secondary y-axis shows the d* values. Large variations in relative density are observed for constant energy density values. Increasing the energy density does help in improving relative density even for same R_m, however, relative densities above 98% are observed only for $d^* > 1$.
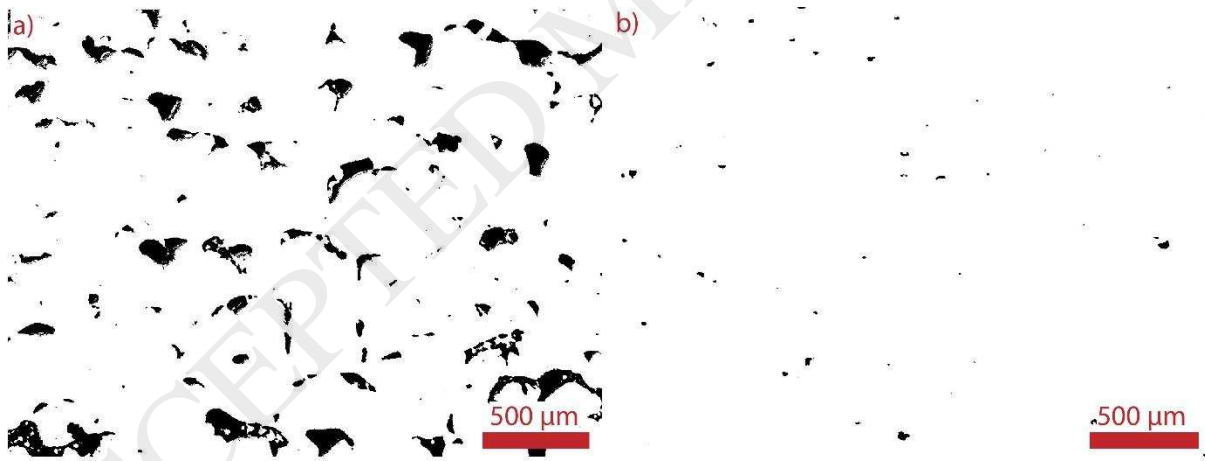

Figure 18: Micrographs showing cross section of Al samples produced with energy density of 173.61 J/mm³. a)$d^* = 0, v = 300 \text{ mms}^{-1}, Q = 125$ W, average porosity 8.1 % b) $d^* = 1.7, v = 900 \text{ mms}^{-1}, Q = 375$ W, average porosity 0.3 %

Table 1: Variable parameters used for trial 1; fixed parameters: $p = 50$ μm, $l = 30$ μm, $Q = 143$ W and $d^* = 0$

Sample ID	1A1	1A2	1A3	1B1	1B2	1B3	1C1	1C2	1C3
h (μm)	45	45	45	50	50	50	55	55	55
t_e (μs)	100	150	200	100	150	200	100	150	200
Mean % porosity	12.82	12.08	12.85	12.33	11.35	15.70	12.93	13.05	13.30

Table 2: Variable parameters used for trial 2; fixed parameters: $t_e = 150$ μs, $l = 30$ μm and $Q = 143$ W

Sample ID	2A1	2A2	2A3	2B1	2B2	2B3	2C1	2C2	2C3
h (μm)	35	35	35	45	45	45	55	55	55
p (μm)	25	35	45	25	35	45	25	35	45
d^*	0.785	0.639	0.389	0.628	0.431	0.000	0.342	0.000	0.000